JTTEE5 17:865–871
DOI: 10.1007/s11666-008-9224-y
1059-9630/$19.00 © ASM International

Thermally Sprayed $CaZrO_3$ Coatings

E. Garcia, C. Cano, T.W. Coyle, M.I. Osendi, and P. Miranzo

(Submitted May 14, 2008; in revised form July 31, 2008)

A comparative study of $CaZrO_3$ coatings prepared by air plasma and flame spray processes is presented. The microstructural characteristics and phases were analyzed and discussed as a function of the spraying temperature achieved with each technique. Vickers hardness tests performed on polished cross sections of the different coatings were used to estimate their porosity. Thermal diffusivity values measured on freestanding thick coatings (500 μm) using the laser flash technique were very low and depended strongly on the pore shape. Crystallization was promoted by treating the coatings at 1200 °C, and the results are explained with aid of the ZrO_2-CaO equilibrium phase diagram.

Keywords calcium zirconate, flame spray, hardness, microstructure, plasma spray, thermal barrier coatings, thermal conductivity

1. Introduction

Thermal spraying includes several powerful processing techniques for producing coatings of diverse types such as wear and erosion resistant coatings, protective coatings against oxidation and corrosion, and thermal barrier coatings for high temperature environments. In most of these processes, particles are injected into a high temperature gas where they are heated, melted, accelerated, and sprayed onto a prepared substrate. The temperature distribution in the torch and the particle velocities depend on the particular technique used, both parameters affecting the final microstructure and the properties of the coatings (Ref 1).

Flame spraying (FS) is a widely and commercially used method for low-energy consuming processes that can be adapted to several combinations of gases, such as acetylene, propane, hydrogen, together with oxygen. Flame spray uses the thermal energy released during the combustion of fuel gases to generate heat. The oxy-acetylene torches are the most common, using acetylene as the main fuel in combination with oxygen to generate the highest combustion temperatures.

Atmospheric plasma spray (APS) uses the energy of the ionized plasma forming gas produced by an electric arc as the heating source. In this case, the temperature is higher than that produced by the oxy-acetylene flame spraying. Therefore, higher melting point materials can be deposited by atmospheric plasma spraying. This technique also provides higher particle velocities (800 m s^{-1}) than those achieved by flame spraying (below 100 m s^{-1}) (Ref 2, 3).

The production of thermal barrier coatings (TBCs) by these techniques is of considerable importance in applications such as aerospace and aircraft engines, advanced gas turbines, and diesel engines components. By using TBCs on high temperature components, the efficiency of the industrial processes can be increased due to the higher operating temperatures and reduced cooling air requirements. In the same way, the lifetime of the coated components is prolonged due to the lower metal surface temperatures.

The material commonly used in TBCs has been yttria-stabilized zirconia (7 wt.% Y_2O_3), mainly because of its low thermal conductivity, high thermal expansion coefficient, and good erosion resistance (Ref 4). In comparison, calcium zirconate ($CaZrO_3$) has high thermal and chemical stabilities, and good thermal shock resistance, rendering this to be a convenient candidate for some thermal barrier coating applications (Ref 5). In addition, due to the perovskite-type structure of $CaZrO_3$, a low thermal conductivity can be expected (Ref 6-8). Compared to YSZ, $CaZrO_3$ has a lower melting point (2550 °C), which allows its processing not only by atmospheric plasma spraying but also by flame spraying deposition technique.

In the present work, the properties and microstructures of coatings produced by the two different spraying processes, flame spraying (FS) and atmospheric plasma spray (APS), were compared. These coatings were analyzed in terms of microstructure, phases, composition, hardness, porosity, and thermal conduction properties. Post-heat treatments were carried out to evaluate the phase evolution and the properties of the coatings.

This article is an invited paper selected from presentations at the 2008 International Thermal Spray Conference and has been expanded from the original presentation. It is simultaneously published in *Thermal Spray Crossing Borders, Proceedings of the 2008 International Thermal Spray Conference*, Maastricht, The Netherlands, June 2-4, 2008, Basil R. Marple, Margaret M. Hyland, Yuk-Chiu Lau, Chang-Jiu Li, Rogerio S. Lima, and Ghislain Montavon, Ed., ASM International, Materials Park, OH, 2008.

E. Garcia, C. Cano, M.I. Osendi, and **P. Miranzo**, Institute for Ceramics and Glass (C.S.I.C.), C/Kelsen 5, Campus de Cantoblanco, Madrid 28049, Spain; and **T.W. Coyle**, Centre for Advanced Coating Technologies, University of Toronto, Toronto, ON, Canada M5S 3E4. Contact e-mail: garcia@icv.csic.es.

2. Experimental Procedure

The coatings were deposited over AISI 304 stainless steel substrates. The surface of the substrates was grit-blasted with corundum particles having a mean particle size of 530 μm to get a maximum roughness of 27.6 ± 2.4 μm. The ceramic feedstock was commercial calcium zirconate ($CaZrO_3$) (Metaceram 28085, Eutectic Castolin, Spain) with an average particle size of 47.9 μm.

The FS coatings of $CaZrO_3$ were achieved using an oxygen-acetylene gun (model CastoDyn DS 8000, Eutectic Castolin, Spain). The torch input power was 28 kW and the powder feed rate was ~20 g min^{-1}. The standoff distance was fixed at 15 cm according to previous experiments (Ref 9).

The plasma gun is a homemade gun developed at the Centre for Advanced Coating Technologies of the University of Toronto (CACT) (Ref 10). The plasma forming gases were CO_2/CH_4 mixtures, giving an output power of 40 kW. The coatings were deposited at standoff distances of 10, 17, and 22 cm with a feed rate of 17 g min^{-1}. The substrates were air-cooled during deposition.

In-flight particle properties were measured for the APS processes with a DPV 2000 monitoring system (Tecnar, Canada) to establish interrelations between spraying parameters and particle in-flight properties.

The microstructures of the coatings were analyzed on polished cross sections and on top surfaces by scanning electron microscopy (SEM) (DMS-950 Carl-Zeiss, Germany). Quantitative compositions were calculated by energy-dispersive x-ray spectroscopy (EDS) from standardless point analyses, using Proza φ(ρz) corrections. The crystalline phases in the specimens were identified by x-ray diffraction analysis (XRD) (Siemens D5000, Germany) performed on the coating surface. Chemical analyses were done using an x-ray fluorescence spectrometer (PW-2424, Philips, NL) equipped with an ultrathin window x-ray tube and high power (2.4 kW) rhodium anode. The hardness of the ceramic coatings was measured on the polished cross section of the specimens by microhardness Vickers indentation using loads of 1.9 and 2.9 N for 15 s (ZHU 2,5; Zwick GmbH & Co. KG, Germany). At least 5 measurements were taken for each coating.

Porosity, θ, was calculated from hardness using the following expression (Ref 11):

$$\frac{H}{H_0} = (1-\theta)^2 e^{-\beta\theta} \quad \text{(Eq 1)}$$

where H is the measured hardness, H_0 is the hardness for the dense material (10.7 GPa (Ref 12)), and β is a constant parameter that depends on the material. The same β parameter calculated for a ZrO_2/Ni coating was used, which was 2.6, as it has been proved to be valid by comparing to imaging analysis data for the present case (Ref 12).

Thermal diffusivity (α) of freestanding coatings was measured using the laser-flash technique (Thermaflash 2000, NESTCH group, MA, USA). The thermal conductivity (k) was obtained through the expression $k = \alpha \cdot \rho \cdot C_p$, where ρ is the coating density and C_p is the heat capacity of the ceramic material taken from thermodynamic tabulated sources (Ref 13).

3. Results and Discussion

Adherent porous coatings were obtained by both methods (FS, APS) with thicknesses between 200 and 400 μm. The average temperatures and velocities of the APS particles at the different standoff distances are shown in Table 1. The highest average temperature (3028 ± 279 °C) and velocity (238 ± 114 m s^{-1}) were reached for the shorter standoff distance (10 cm, APS_10).

3.1 As-Sprayed Coatings

An example of the cross sections of the coatings can be seen in Fig. 1. Both types of coatings are porous but

Table 1 Average temperatures and velocities measured for the APS particles at the different standoff distances

	Standoff distance, cm	Temperature, °C	Velocity, m s^{-1}
APS_10	10	3028 ± 279	238 ± 114
APS_17	17	2598 ± 175	155 ± 51
APS_22	22	2504 ± 75	97 ± 21

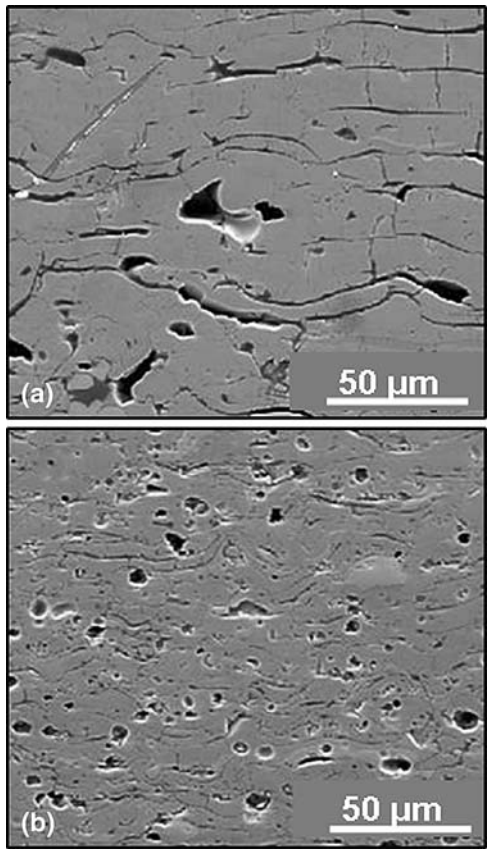

Fig. 1 SEM micrographs of polished cross sections of microstructures of the coatings for both spray processes: (a) FS coating with neutral flame, (b) APS coating sprayed at 17 cm

present different morphologies. The coating obtained by the FS process (Fig. 1a) exhibits a structure with thicker lamellas compared to the APS_17 coating (Fig. 1b). The microstructures of the APS coatings were similar for the three standoff distances and all contain more spherical pores of larger size than those observed in the FS coating.

A comparison of the top surfaces of both $CaZrO_3$ coatings is shown in Fig. 2. The FS coating (Fig. 2a) had a very smooth top surface with a few unmolten particles. The APS $CaZrO_3$ coatings (Fig. 2b) evidenced a rougher top surface and, apparently, higher level of porosity. No appreciable differences among the APS coatings were observed, although probably more overheated particles could be expected for the coating sprayed at 10 cm.

The morphology of the APS coatings indicates formation of bubbles in the splats (Ref 14, 15). During the particle impinging and flattening steps, entrapped hot gases can expand and escape through the flattened particles. Depending on the flattening particle viscosity at impact and the escaping gas energy, the gases could completely pass through the flattening particle generating volcano-sort-bubbles (Ref 16).

The x-ray diffraction patterns recorded for the original $CaZrO_3$ powder and for the coatings sprayed with both processes are shown in Fig. 3. The diffraction patterns showed that all analyzed samples contained orthorhombic $CaZrO_3$. Peaks that can be associated to cubic ZrO_2 phase were also clearly found in the APS coatings, although small ZrO_2 peaks were also found in the FS coating. Some preferential orientation was observed on the XRD pattern of the FS coating as there was an increase in the intensity of the peaks corresponding to the (101) and (202) $CaZrO_3$ planes, compared to that of the (121) plane (Ref 9). The APS coatings did not show a preferential orientation since the $I_{(101)}/I_{(121)}$ ratio was somewhat similar to that of the original powder. This less important texture effect can also be observed at the microstructure level (Fig. 4). While a columnar growth was observed inside the splats for the FS coatings (Fig. 4a), the APS coatings presented only a piling up of thin splats (Fig. 4b). This fact could be explained by the faster cooling rate of the splats in the APS, due to the air-cooling of the substrates, as compared to the FS, where no forced cooling was employed.

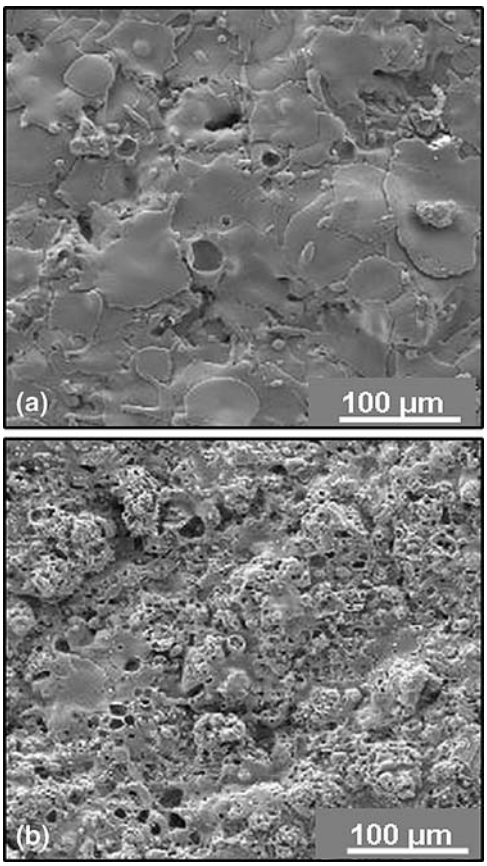

Fig. 2 Micrographs of the coatings top surface for both the processes: (a) FS coating (b) APS coating sprayed at 17 cm

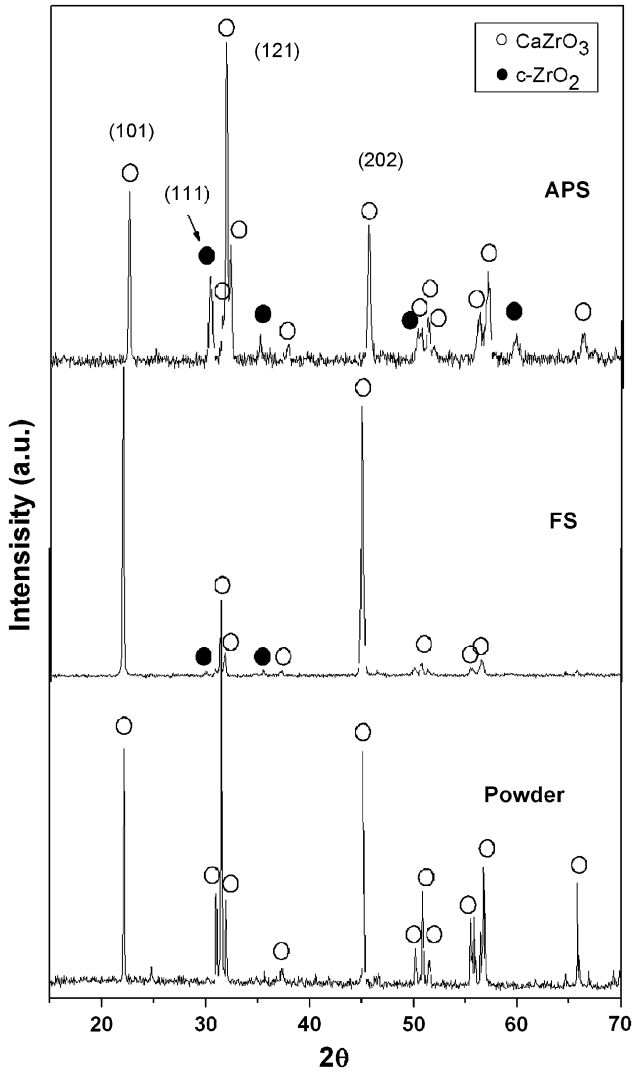

Fig. 3 XRD patterns of the $CaZrO_3$ coatings deposited by APS and FS processes and the original powder

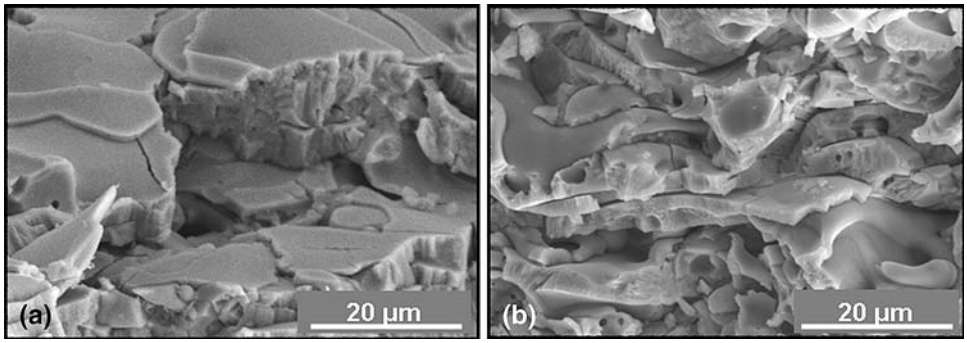

Fig. 4 Fresh fracture micrograph of FS (a) and APS (b) coatings

Table 2 Chemical composition of FS and APS coatings measured by x-ray fluorescence (XRF)

Compound	Feedstock powder, wt.%	FS coating, wt.%	APS coating, wt.%
CaO	30.0	29.7	27.6
MgO	0.29	0.26	0.19
SiO_2	0.52	0.48	0.20
ZrO_2	67.7	67.8	70.1

The relatively higher amount of c-ZrO_2 observed in the APS coatings, compared to the FS coating, can be associated to the CaO volatilization caused by the higher temperatures and reducing atmosphere generated by the CO_2/CH_4 plasma during spraying. This CaO volatilization was confirmed by the x-ray fluorescence (XRF) chemical analyses given in Table 2. About 3 wt.% reduction in CaO concentration was observed in the APS coating, whereas the FS coating showed similar composition to the starting calcium zirconate powders.

As seen in Fig. 5, the microstructure of the coatings showed areas of different gray levels. The average EDS analyses corresponding to those phases showed significant differences on the ZrO_2 and CaO mol.% content. The different compositions related to these phases have been localized in the ZrO_2-CaO phase equilibrium diagram (Ref 17), shown in Fig. 6, to aid the discussion. The matrix main phase (CZ in Fig. 5) has a composition 50:50 mol.% ZrO_2:CaO (Fig. 6, area ''CZ''), and therefore, it would correspond to the calcium zirconate identified by XRD. Dark gray phases were found in FS coating (''D'' in Fig. 5a), but not in APS coatings. These phases presented compositions with up to 10% of other elements such as aluminum and silicon, although maintaining the same ZrO_2:CaO ratio of ~1. Therefore, these could be identified as amorphous metastable phases that on equilibrium will crystallize on $CaZrO_3$. These phases are not detected for APS coatings because SiO_2 volatilization occurs in these coatings (Table 2). Finally, the main differences among coatings refer to the amount and composition of the clearest phases (C). Those had enriched ZrO_2 compositions with CaO contents ranging from 41 to 20 mol.%, extending from the eutectic point of the system (41 mol.%) down to the limit of CaO solid solution in c-ZrO_2 (Fig. 6 area ''C-a''). The largest standoff distance of APS coatings showed composition with even lesser CaO content, in the range 0-6 mol.% (Fig. 6 area ''C-b''). According to the XRD analyses and the information supplied by the corresponding phase equilibrium diagram, clear phases with CaO content less than 20 mol.% may be associated to crystalline c-ZrO_2, whereas those with CaO contents >20 mol.% would be amorphous metastable phases.

The presence of ZrO_2-enriched phases was explained because the volatilization of CaO in the coatings was a local phenomenon, which depended on the location of the particles inside the flame or plasma torch. The APS 22 cm coating showed the lowest CaO content because $CaZrO_3$ particles are inside the high temperature plasma plume for a longer time before reaching the substrate, which promoted higher volatilization of the CaO.

The average microhardness and porosity values measured in all $CaZrO_3$ coatings for both the FS and APS processes are provided in Table 3. The FS coating showed a slightly higher hardness value than the APS coatings. This result is consistent with the higher porosity measured for the APS coatings. No appreciable differences in hardness or porosity were found among APS coatings deposited at different standoff distances.

The thermal conductivity data obtained for all coatings were lower than those typically reported in the literature for ZrO_2-based TBCs (Ref 18, 19). This could be explained not just by the porosity amount but also by the pore shape (Ref 20). The FS coating is remarkable since, having a lower porosity, its thermal conductivity is much less than in the APS coatings. One possible cause is the different microstructure of both coatings (Fig. 1). Longer intersplat pores were found in the case of the FS coatings, which means that the heat propagation through this coating is hindered as compared to the APS coatings.

3.2 Heat-Treated Coatings

FS, APS_10, and APS_22 coatings were subjected to thermal treatments at 1200 °C during 12 h, to study phase and properties evolution. As there are not significant differences in the microstructures of the APS coatings, only the longest and shortest standoff distances have been selected for the heat treatments. The microstructure of the heat-treated coatings was characterized by the presence of

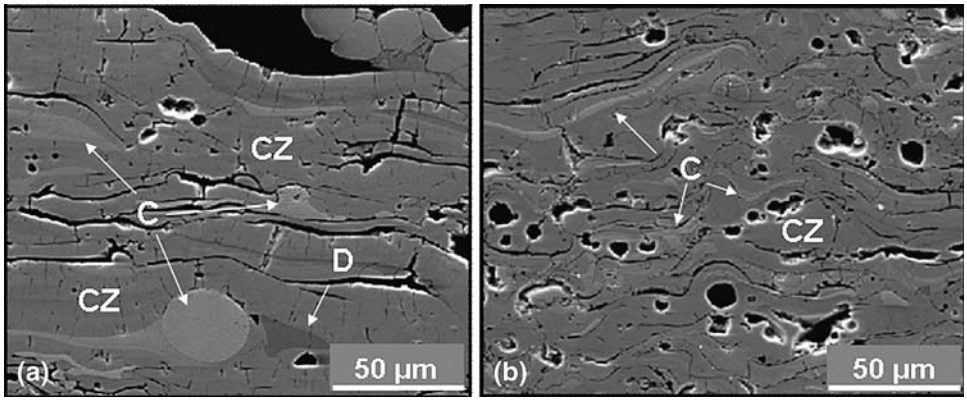

Fig. 5 SEM micrographs of details of the microstructure of FS (a) and APS (b) coatings. "CZ" shows matrix regions of $CaZrO_3$ composition, "C", clear phases, and "D" dark phases

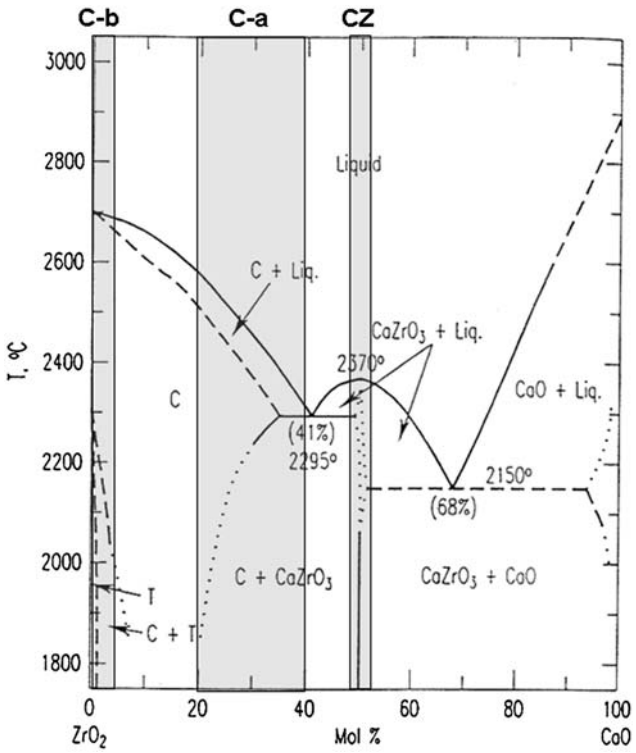

Fig. 6 ZrO_2-CaO phase equilibrium diagram (Ref 17). The shadowed areas are related with the different phase compositions found throughout the coatings

longer intersplat cracks (Fig. 7) compared to the untreated coating (Fig. 1), especially for the APS coatings. A crystallization process with micropores formation is clearly observed at higher magnification (Fig. 7c, d) This crystallization probably involves volume changes and then is likely responsible for the increase in the intersplat crack length.

The XRD analysis identified a small relative increase of the cubic ZrO_2 peaks compared to the $CaZrO_3$ peaks in all the treated coatings (Table 4). When melted particles reach the substrate at very high temperature, they remain partially amorphous; and then, crystallize later on c-ZrO_2 and $CaZrO_3$ when the coating is annealed at 1200 °C. Although no differences in crystalline phases were observed among the different coatings by XRD, the as-sprayed FS coating seemed to be more crystalline as it showed less degradation after heat-treating (Fig 7). This is a consequence of the lower temperatures and slower cooling rates reached by the particles.

In Table 3, the hardness values obtained for the heat-treated samples are also shown. The reduction in more than 25% of the corresponding original value is noticeable. The increase of the intersplat cracks length and the increase in apparent total porosity of the coatings could be the main reason for this reduction.

4. Conclusions

$CaZrO_3$ coatings produced by flame and air plasma spray techniques present different microstructures and

Table 3 Vickers microhardness, porosity, and thermal conductivity measured at room temperature of as-sprayed coatings and Vickers microhardness and porosity of heat-treated coatings

	As-sprayed coatings			Heat-treated coatings, 1200 °C	
	Microhardness, GPa	Porosity, vol.%	Thermal conductivity, $Wm^{-1} K^{-1}$	Microhardness, GPa	Porosity, vol.%
FS	4.8 ± 1.5	16.5	0.29	2.9 ± 0.6	26.5
APS (10 cm)	4.2 ± 1.0	19.2	0.72	3.1 ± 0.9	25.2
APS (17 cm)	4.2 ± 1.1	19.2	0.91	-	-
APS (22 cm)	4.6 ± 1.0	17.4	0.80	2.4 ± 1.2	30.0

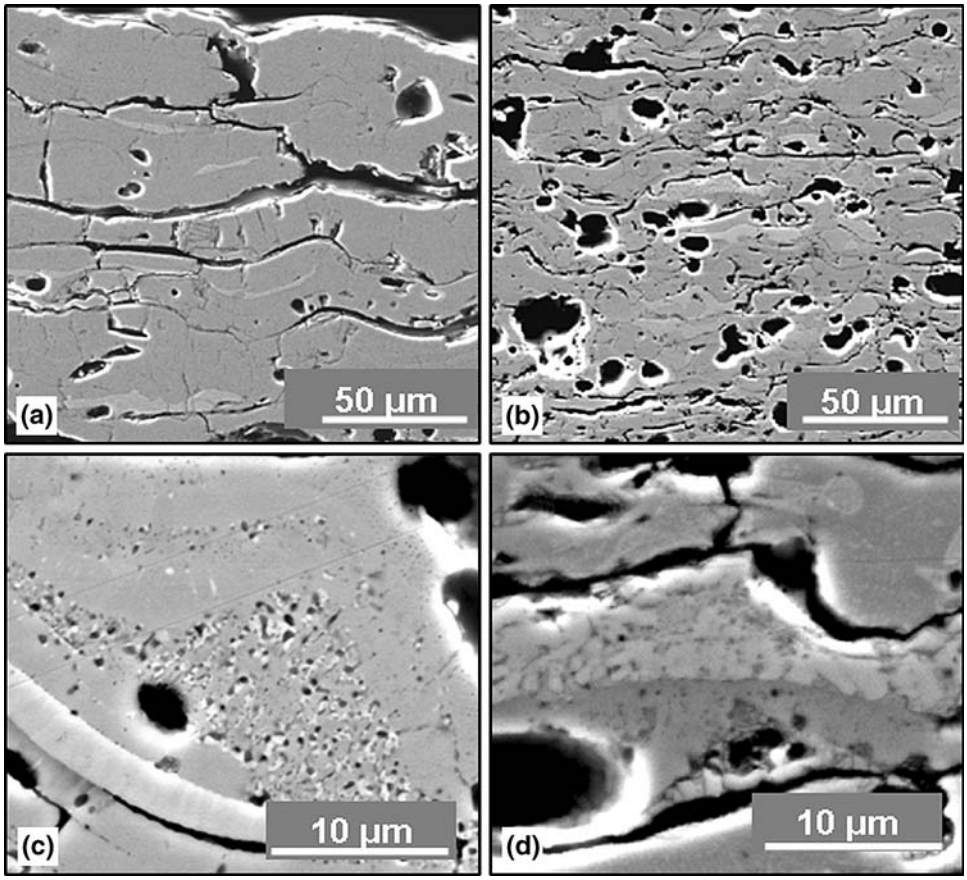

Fig. 7 Micrographs of the heat-treated FS (a, c) and APS 22 cm sprayed coatings (b, d)

Table 4 XRD peak intensity ratios of the c-ZrO_2 (111) and $CaZrO_3$ (121) diffraction planes obtained for the as-sprayed and heat-treated coatings

	I_{ZrO_2}/I_{CaZrO_3}	
	As-sprayed coatings	**Heat-treated coatings, 1200 °C**
FS	0.25	0.37
APS_10	0.33	0.38
APS_22	0.25	0.33

properties. All of them are porous, but flame sprayed coating shows longer intersplat cracks and APS coatings larger round pores. They are formed by a major matrix of CaO:ZrO_2 with a composition close to that of o-$CaZrO_3$ (50:50 mol.%), and other ZrO_2-enriched minor phases, which is the consequence of a preferential volatilization of CaO. Some of the latter have compositions with CaO contents within the solid solution limit of the Ca-ZrO_2. Phases with compositions in the range 20-40 mol.% CaO are identified mainly as amorphous metastable phases.

All the $CaZrO_3$ coatings show very low thermal conductivity, which is very attractive for their use as TBCs, much lower in FS than in APS coatings due to the particular microstructure of intersplat cracks.

The thermal treatments at 1200 °C induce some crystallization of the amorphous phases present in the coating, modifying the microstructure and the mechanical properties. This process is more significant in the APS coatings because they were more amorphous as sprayed.

Acknowledgments

The authors would like to acknowledge the financial support from the MEC-MAT2006-7118. E. Garcia acknowledges financial support from the I3P-PC2005L program. Thanks are given to F.J. Valle for ED-XRF analyses.

References

1. R.B. Heimann, *Plasma Spray Coatings, Principles and Applications*, VCH, Weinheim, New York, USA, 1996
2. J.R. Davis, *Handbook of Thermal Spray Technology*, ASM International, Materials Park, OH, EEUU, 2004
3. L. Pawlowski, *The Science and Engineering of Thermal Spray Coatings*, Ed. John Wiley & Sons Ltd., Chichester, UK, 1995
4. P.G. Klemens and M. Gell, Thermal Conductivity of Thermal Barrier Coatings, *Mater. Sci. Eng. A Struct.*, 1998, **245**, p 143-149
5. A. De Petris, F. Ricciardiello, and O. Sbaizero, Mechanical Properties of Polycrystalline $CaZrO_3$, *Powder Metall. Int.*, 1986, **18**, p 427-443

6. D.R. Clarke and S.R. Phillpot, Thermal Barrier Coating Materials, *Mater. Today*, 2005, **8**, p 22-29
7. S. Yamanaka, K. Kurosaki, T. Maekawa, T. Matsuda, S. Kobayashi, and M. Uno, Thermochemical and Thermophysical Properties of Alkaline-Earth Perovskites, *J. Nucl. Mater.*, 2005, **344**, p 61-66
8. P.S. Murti and M.V. Krishnaiah, Investigation of the Thermal Conductivity of Calcium Cerate and Calcium Zirconate, *Mater. Chem. Phys.*, 1992, **31**, p 347-350
9. C. Cano, M. Belmonte, M.I. Osendi, and P. Miranzo, Effect of the Type of Flame on the Microstructure of $CaZrO_3$ Combustion Flame Sprayed Coatings, *J. Surf. Coat. Technol.*, 2007, **201**, p 3307-3313
10. L. Pershin, L. Cheng, and J. Mostaghimi, Comparison of Molecular and Argon Gases for Plasma Spraying, *Thermal Spray 2007: Global Coating Solutions*, B.R. Marple, M.M. Hyland, Y.C. Lau, C.J. Li, R.S. Lima, and G. Montavon, Ed., ASM International Materials Park, Ohio, USA, e-version
11. R. Polanco, P. Miranzo, and M.I. Osendi, Fabrication and Microstructure of a ZrO_2-Ni Functionally Graded Bonding Interlayer using the Airbrush Spraying Method, *Acta Mater.*, 2006, **54**, p 2215-2222
12. C. Cano, ''Ceramic Coatings for Thermal and Environmental Barrier Applications,'' Ph. D. Thesis, Autonomous University of Madrid, 2008 (Spanish)
13. *Landolt-Börnstein, Thermodynamic Properties of Inorganic Materials*, Scientific Group Thermodata Europe (SGTE), Part I, Springer-Verlag, Berlin-Heidelberg, 1999
14. Y. Tanaka and M. Fukumoto, Investigation of Dominating Factors on Flattening Behaviour of Plasma Sprayed Ceramic Particles, *Surf. Coat. Technol.*, 1999, **120-121**, p 124-130
15. A. Kulkarni, A. Vaidya, A. Goland, S. Sampath, and H. Herman, Processing Effects on Porosity-Property Correlations in Plasma Sprayed Ytria-Stabilised Zirconia Coatings, *Mater. Sci. Eng. A Struct.*, 2003, **359**, p 100-111
16. A.A. Syed, A. Denoirjean, B. Hannoyer, P. Fauchais, P. Denoirjean, A.A. Khan, and J.C. Labbe, Influence of Substrate Surface Conditions on the Plasma Sprayed Ceramic and Metallic Particles Flattening, *Surf. Coat. Technol.*, 2005, **200**, p 2317-2331
17. J.P. Traverse and M. Foex, Studies of the Systems Formed by Zirconium with Lime and Strontium Oxide, *High Temp. High Pressures*, 1969, **1**, p 409-427
18. J. Wu, X. Wei, N.P. Padture, P.G. Klemens, M. Gell, E. Garcia, P. Miranzo, and M.I. Osendi, Low Thermal Conductivity Rare Earth Zirconates for Potential Thermal Barrier Coating Applications, *J. Am. Ceram. Soc.*, 2002, **85**, p 3031-3035
19. S. Ahmaniemi, P. Vuoristo, T. Mantyla, F. Cernuschi, and L. Lorenzoni, Modified Thick Barrier Coatings: Thermophysical Characterization, *J. Eur. Ceram. Soc.*, 2004, **24**, p 2669-2679
20. A. D. Jadhav, N.P. Padture, E.H. Jordan, M. Gell, P. Miranzo, and E.R. Fuller, Low-Thermal-Conductivity Plasma-Sprayed Thermal Barrier Coatings with Engineered Microstructures, *Acta Mater.*, 2006, **54**, p 3343-3349